

advances.sciencemag.org/cgi/content/full/7/23/eabg0465/DC1

Supplementary Materials for

Structure of the merozoite surface protein 1 from *Plasmodium falciparum*

Patricia M. Dijkman*, Tanja Marzluf, Yingyi Zhang, Shih-Ying Scott Chang, Dominic Helm, Michael Lanzer,
Hermann Bujard, Mikhail Kudryashev*

*Corresponding author. Email: dijkman@biochem.mpg.de (P.M.D.); misha.kudryashev@biophys.mpg.de (M.K.)

Published 2 June 2021, *Sci. Adv.* 7, eabg0465 (2021)
DOI: 10.1126/sciadv.abg0465

The PDF file includes:

- Figs. S1 to S9
- Table S1
- Legend for movie S1
- References

Other Supplementary Material for this manuscript includes the following:

(available at advances.sciencemag.org/cgi/content/full/7/23/eabg0465/DC1)

- Movie S1

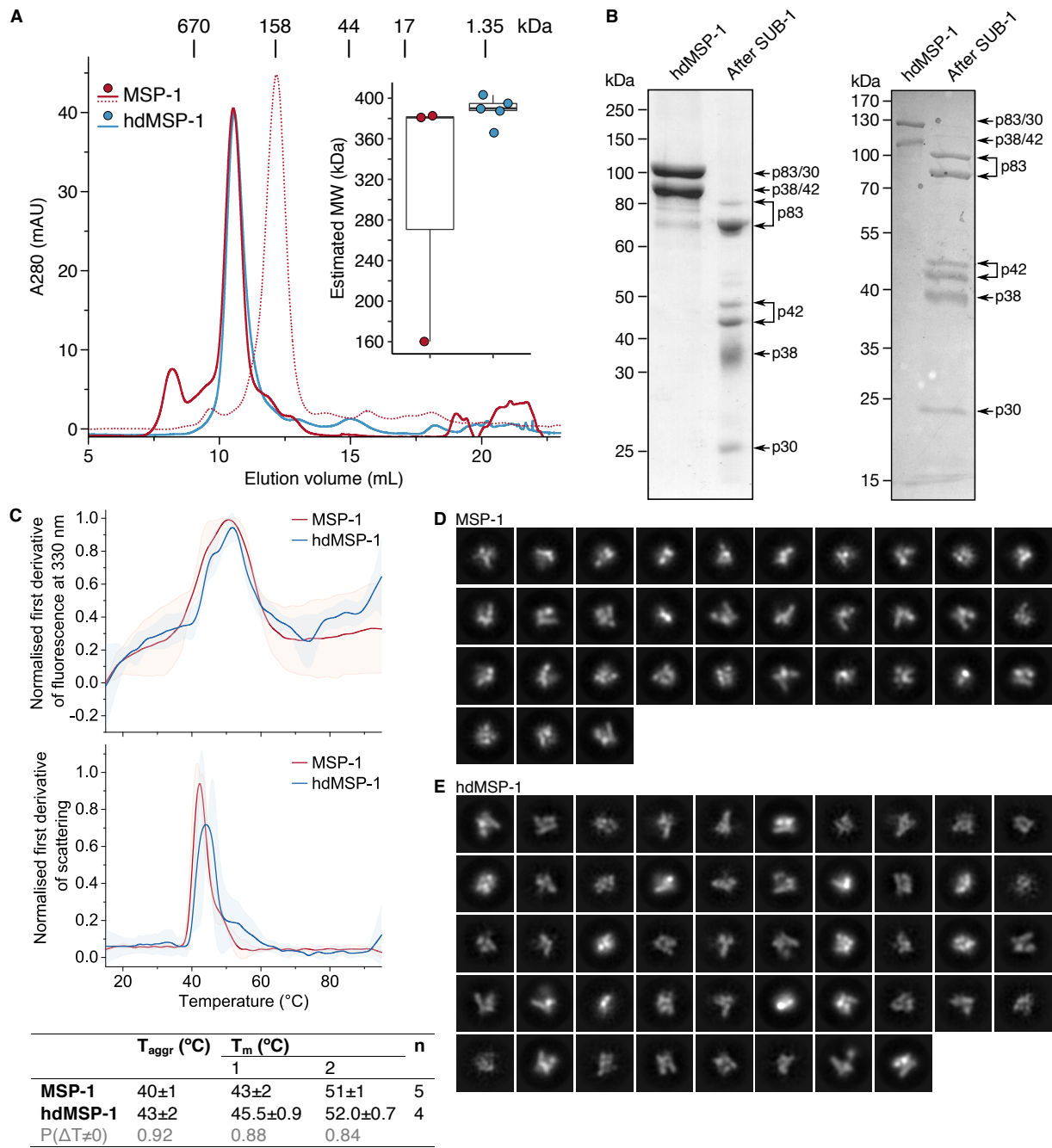
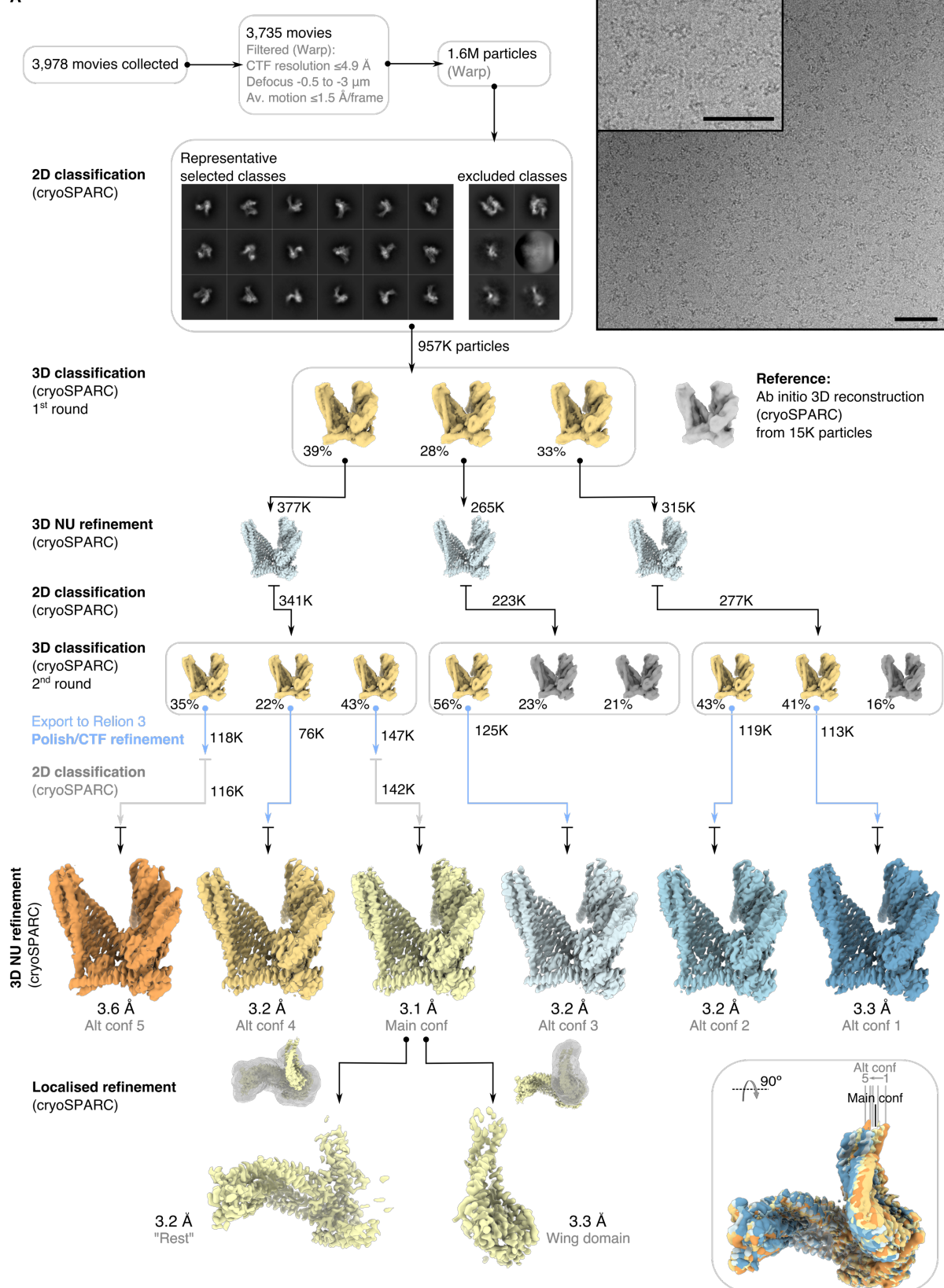


Fig. S1. Characterisation of recombinant (hd)MSP-1. (A) The molecular weight (MW) of the (hd)MSP-1 complexes was estimated by size-exclusion chromatography (SEC); representative chromatograms are shown. The inset shows the estimated MW for different SEC runs. An average of 390 ± 10 kDa ($n=5$) was found for hdMSP-1. Three chromatograms of fully processed MSP-1 resulted in more varying estimates: 160 (dotted red curve), 381 (not shown), and 382 (solid red curve) kDa. The first of these MSP-1 samples was used for cryo-EM structure determination. (B) Coomassie-stained gel of hdMSP-1 before and after in vitro processing with SUB-1. The left gel shows the sample used for cryo-EM structure determination. The right gel shows a sample used for control 2D cryo-EM class averages (fig. S8B), nanoDSF, and MST. Double bands were previously observed for p83 and p42 and attributed to cleavage at non-canonical sites (40). (C) Melting curves for (hd)MSP-1 generated

by nanoDSF. Solid lines represent averages of various runs, while the transparent shading represents the standard deviation. The apparent melting temperature (T_m) was determined from the fluorescence, while the onset of aggregation temperature (T_{aggr}) was determined from the scattering. The probability that the value found for hdMSP-1 differed from that for the fully processed sample ($P(\Delta T \neq 0)$) was estimated using a Bayesian t-test (69); probabilities >0.9 indicate a very likely difference, while probabilities in the range of 0.66-0.9 indicate a likely difference. (D,E) Negative stain 2D class averages of MSP-1 (D) and hdMSP-1 (E) generated in cryoSPARC (42). The samples were diluted to 50 nM prior to grid preparation. Similar classes were obtained for both samples corresponding mainly to the monomeric complex.

A

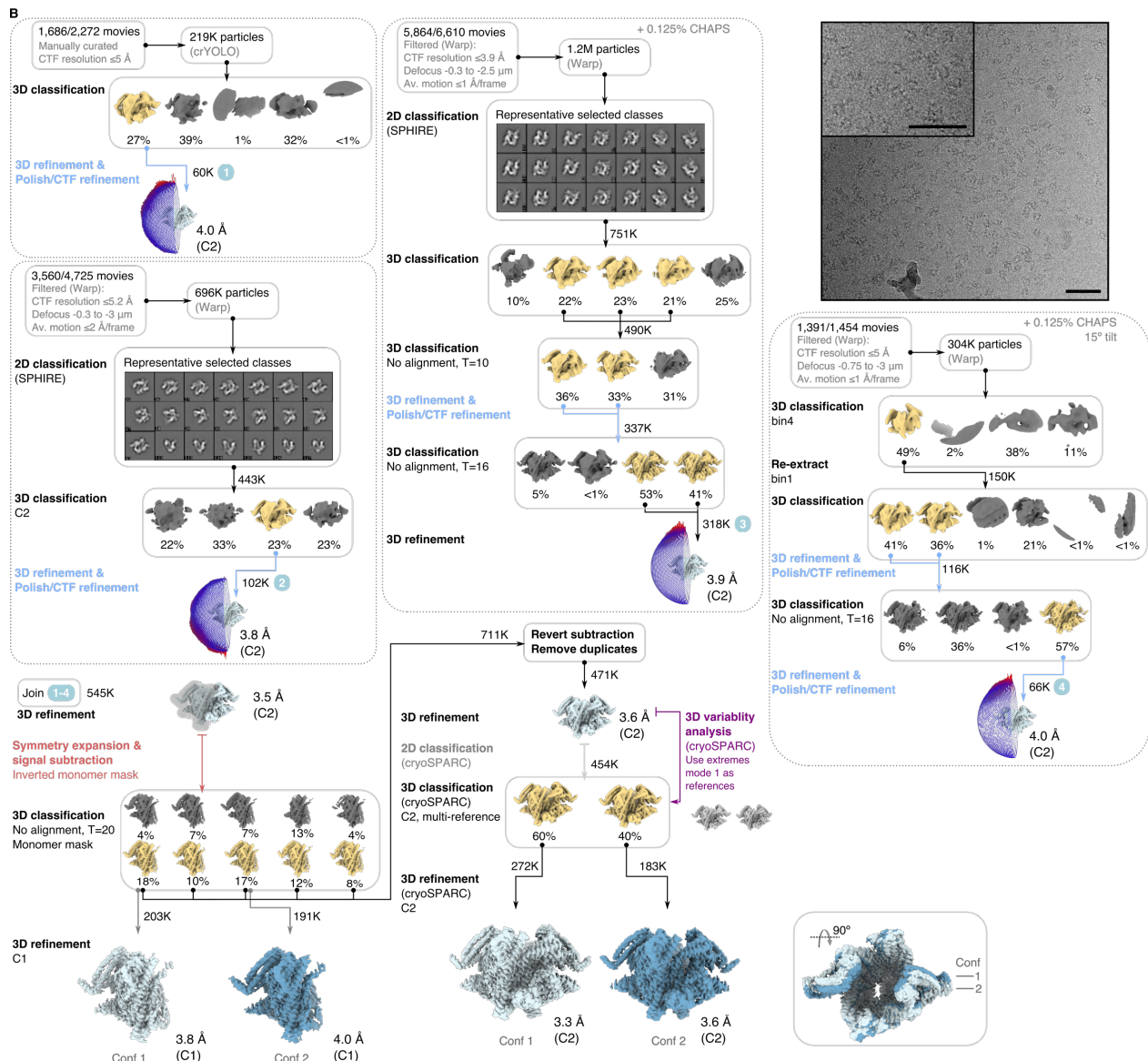


Fig. S2. Processing of (hd)MSP-1 EM data. Graphical representation of processing strategy used for (A) the MSP-1 data set, and (B) the hdMSP-1 data sets. A typical micrograph is shown in the top right corner of each panel (scale bars correspond to 50 nm). Data were processed using RELION 3.0 (43) or different software where indicated (SPHIRE (49) and cryoSPARC (42, 51)). The reconstructed maps had the wrong handedness (as shown here) and were flipped for atomic model building.

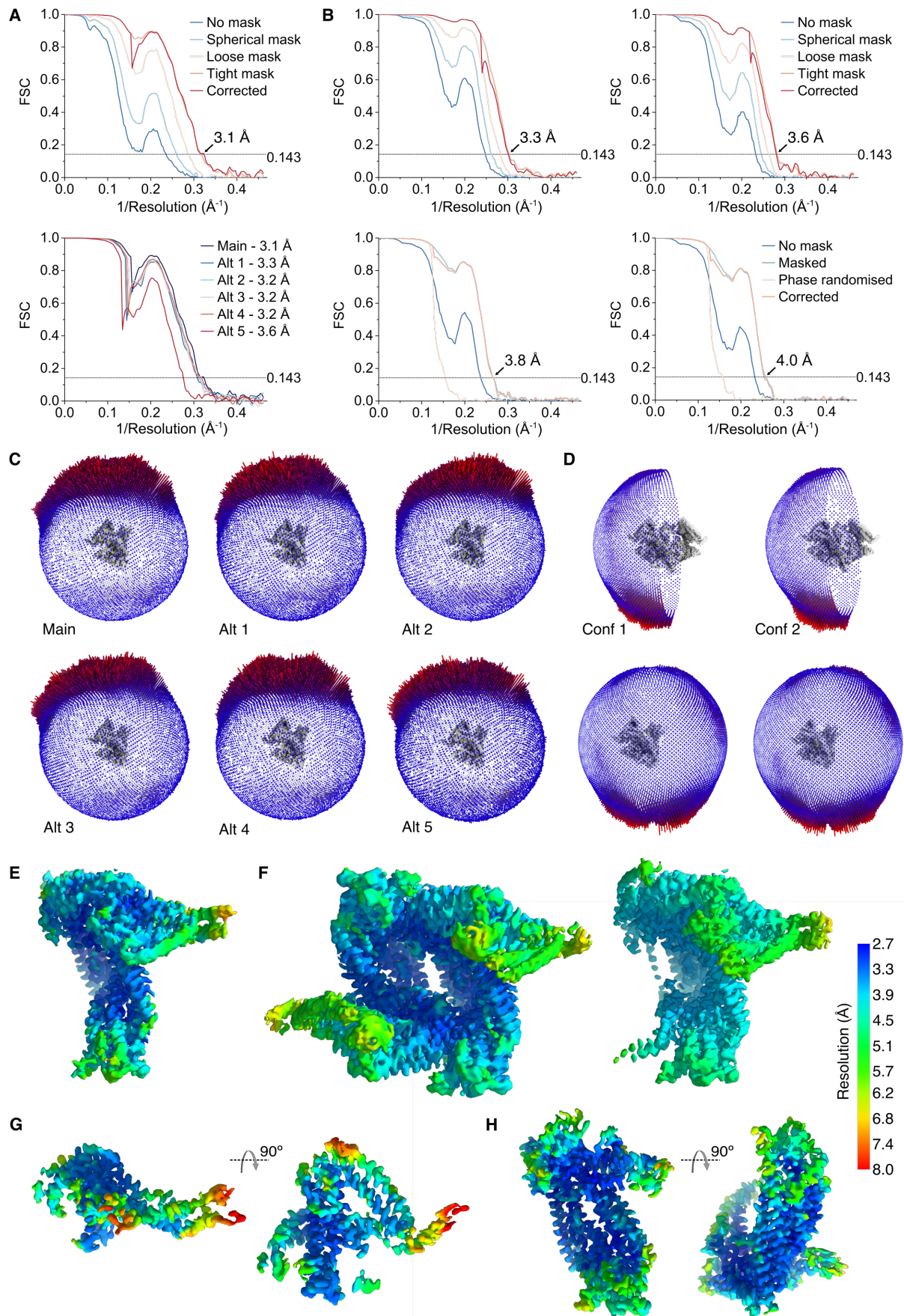


Fig. S3. Resolution of EM maps. (A) Fourier shell correlation (FSC) curves for the reconstruction of the main conformation of MSP-1 with or without applying a mask (top) and

corrected FSC curves for all alternative conformations generated using an auto-tightened mask (bottom) in cryoSPARC (42). (**B**) FSC curves for the hdMSP-1 reconstructions (left: conformation 1; right: conformation 2) for the C2 symmetric reconstructions generated in cryoSPARC (42) (top) and for the symmetry expansion-derived maps generated in RELION 3.0 (43) (bottom). (**C,D**) Angular distribution of particles that contributed to the final MSP-1 (**C**) and hdMSP-1 (**D**) maps. The height of the cylinders is proportional to the number of particles assigned to each view (coloured blue to red for least to most populated views, respectively). Top panel of (**D**) shows the C2 symmetric reconstructions and the bottom panel the symmetry expansion-derived maps. (**E-H**) Local map resolution of (**E**) the main conformation of MSP-1, (**F**) conformation 1 of hdMSP-1 (dimer map and symmetry expansion-derived map), (**G**) locally refined map of the wing domain and (**H**) of the rest of the main conformation of MSP-1. Local resolution was estimated using cryoSPARC (42) or RELION 3.0 (43) for the symmetry expansion-derived map. Due to imperfect signal subtraction, some residual density from the opposing monomer or other domains is still present in the final symmetry expansion-derived monomer map and the locally refined maps, respectively.

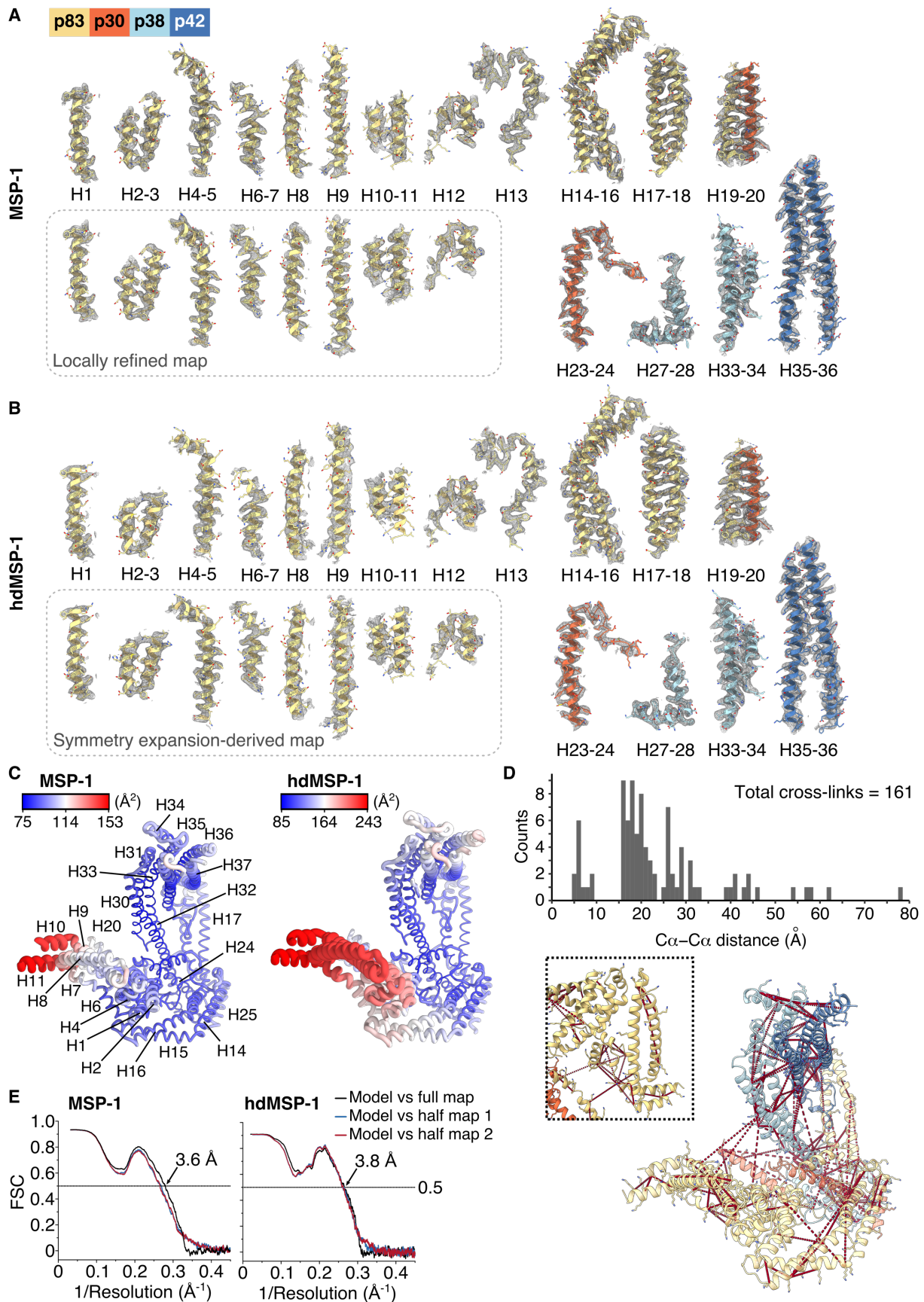


Fig. S4. Map and model quality. (A,B) Representative regions of the built models for (A) MSP-1 and (B) hdMSP-1 and corresponding EM map densities (mesh) auto-sharpened after non-uniform refinement in cryoSPARC (42) or by post-processing in RELION 3.0 (43) with

automatic B-factor determination for the symmetry expansion-derived map. Models are coloured according to MSP-1 subunit (p83, p30, p38, and p42, in yellow, orange, light blue, and darker blue, respectively). **(C)** Model B-factor (a measure of the uncertainty in the location of each atom) plot of the main MSP-1 (left) and hdMSP-1 (right, only one protomer shown) conformations. The relatively high B-factor of helices H8-11 reflects the flexibility of this region, and the resulting uncertainty in the model. **(D)** Cross-linking mass spectrometry (XL-MS) identified 269 cross-links of which 161 could be mapped onto our atomic model; the other cross-links involved lysines in unresolved (loop) regions. Most of the resolved cross-links (88%) fall within the expected <29 Å distance for the cross-linking agent used (70); of the 19 other cross-links, eight involve flexible loop domains, while the other 11 unexplained cross-links (7% of the total cross-links) involve lysines that also take part in (several) other sub-29-Å cross-links. **(E)** Map-model FSC curves of the refined models of MSP-1 (main conformation) and hdMSP-1 (conformation 1). FSC curves are shown for each model versus the full map that it was refined against (black); for the model refined against the first of the two half maps versus that same half map (blue); and of the model refined against the first of the two half maps versus the second of the half maps (red).

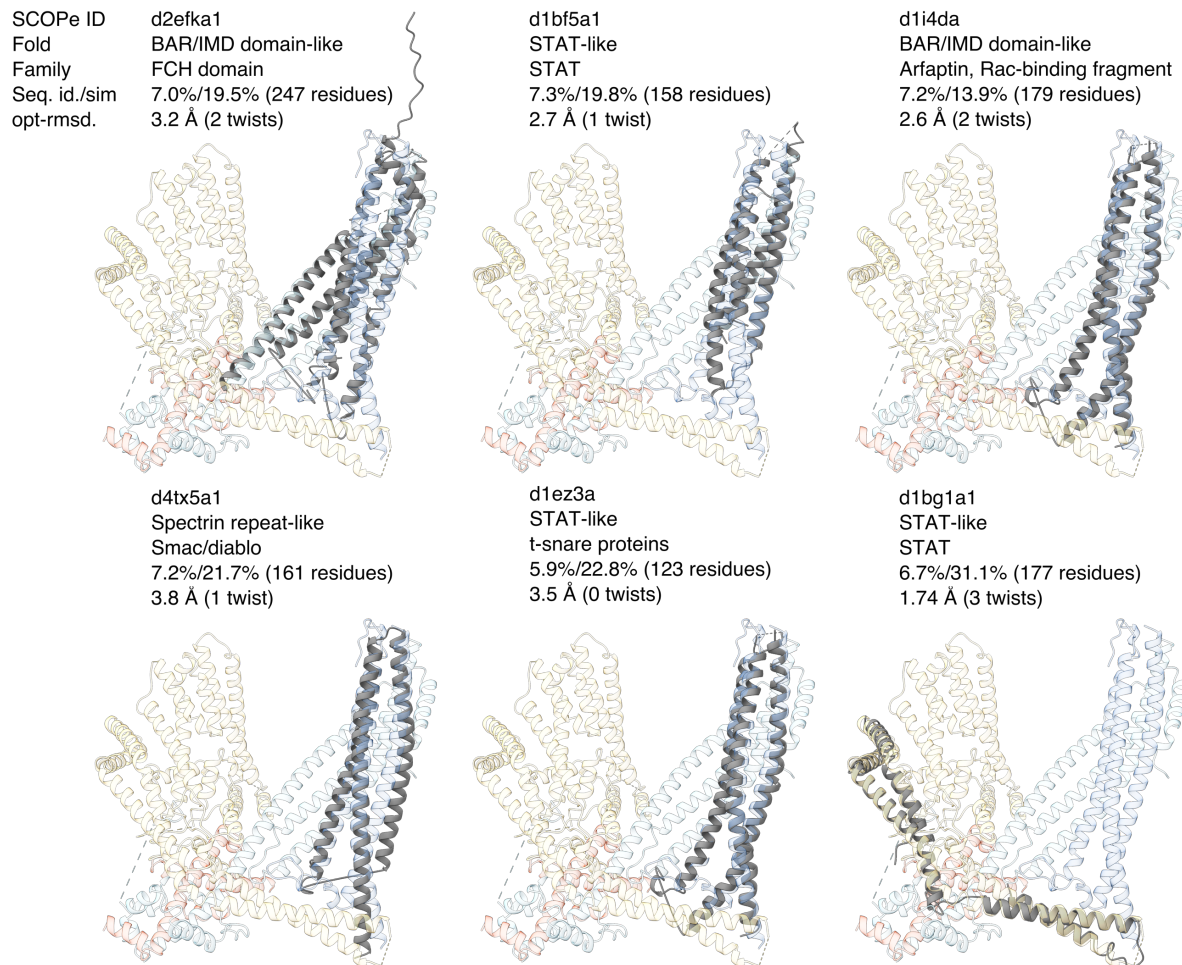
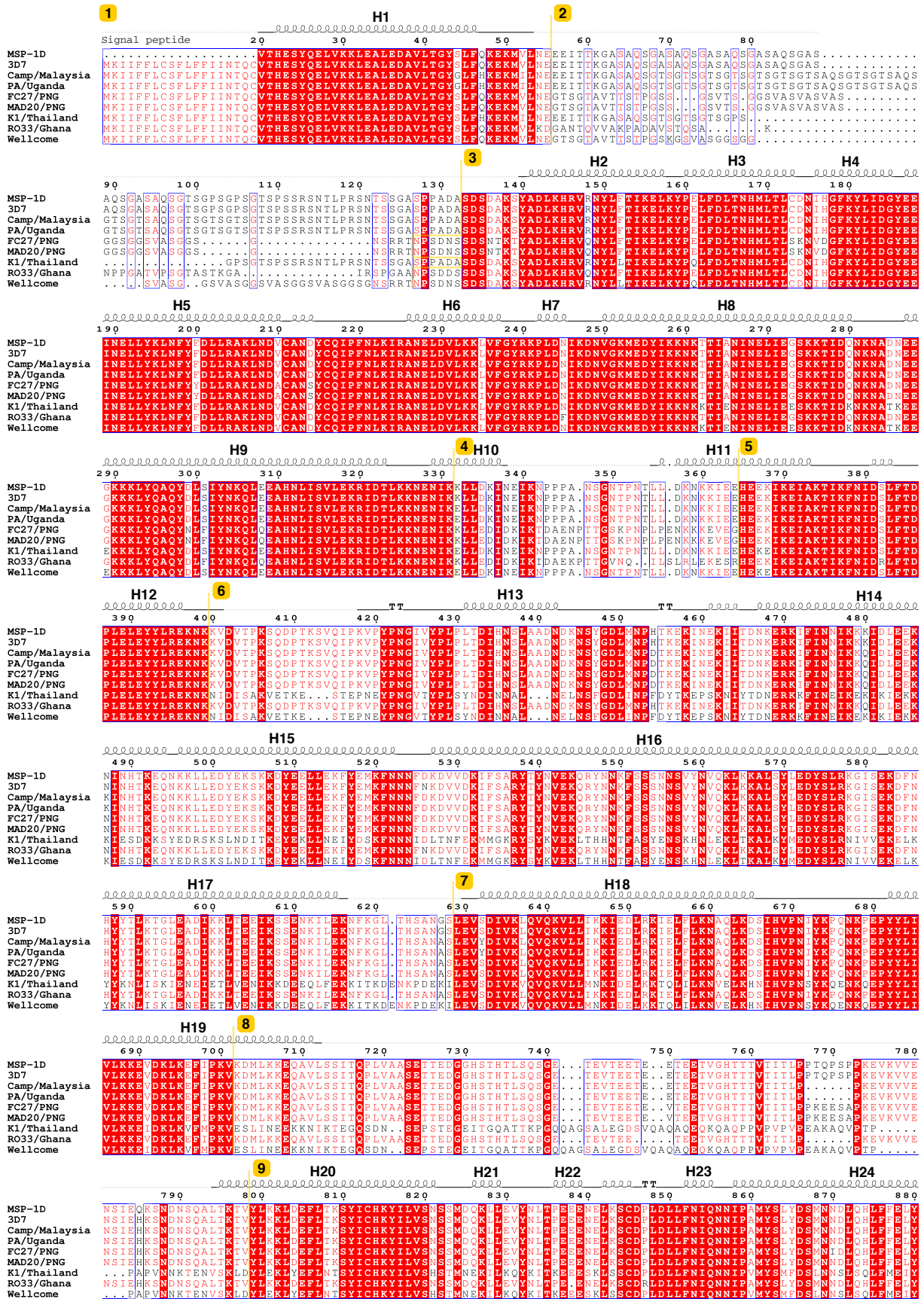


Fig. S5. Flexible structure alignment. Flexible structure alignment (31) of the main conformation of MSP-1 against the SCOPe (structural classification of proteins - extended) database identified several hits for the coiled-coil domain, although sequence identity (seq. id.) and similarity (seq. sim.) were low. Identified folds are shown in grey superimposed onto the main MSP-1 conformation. The top hit (lowest p-value) was a BAR/IMD domain-like fold, which is associated with membrane and cytoskeleton interactions. Other top-10 hits (for folds of >100 residues with three or fewer twists introduced) include STAT-like folds, and a spectrin repeat-like fold. A STAT-like fold was also identified for the coiled-coil H14-18 of p83 (bottom right panel). The root-mean-square deviation of the Ca atoms of the aligned structures (opt-rmsd) is listed, as well as the number of twists introduced in the flexible alignment, and aligned number of residues excluding gaps (31).



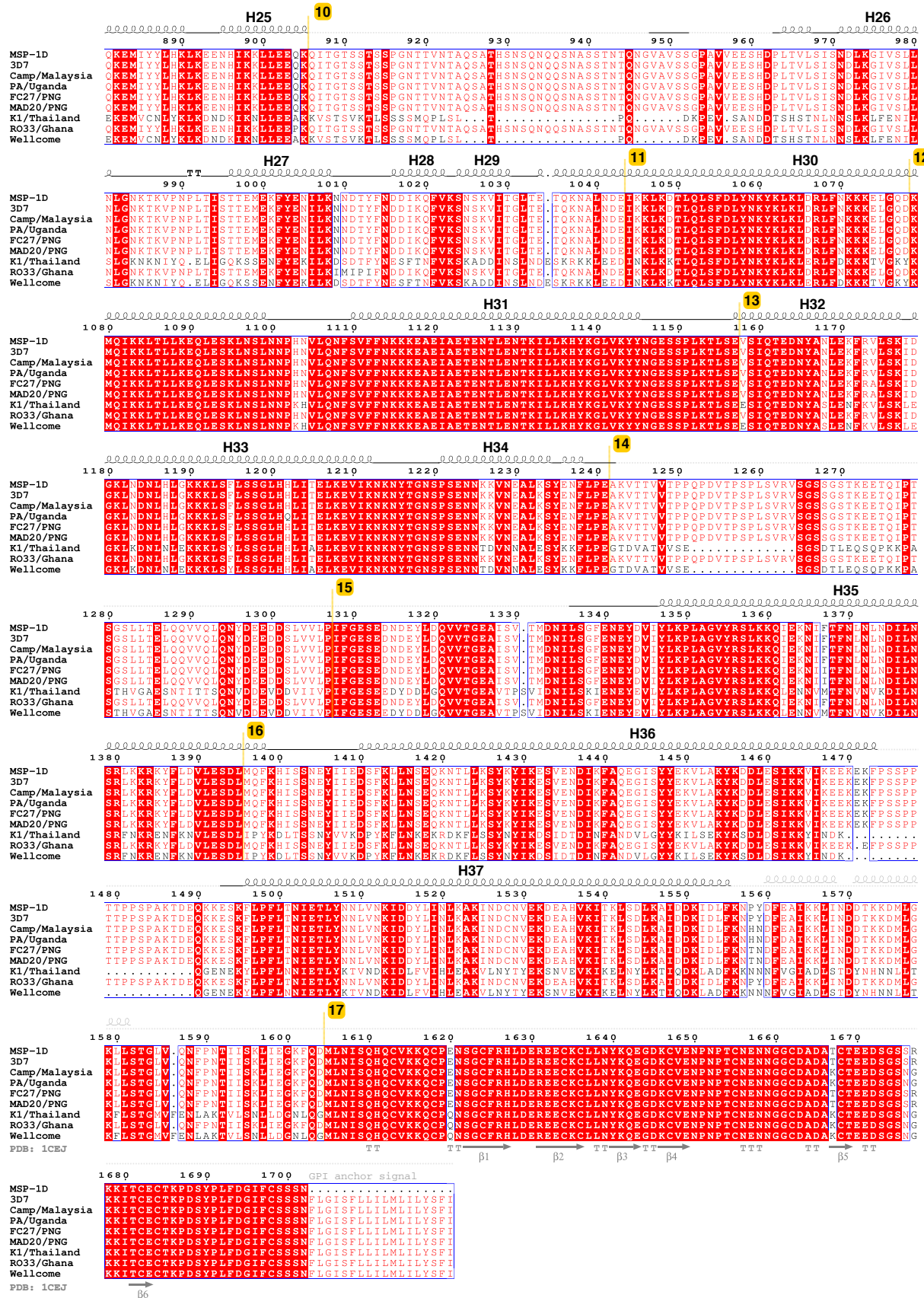
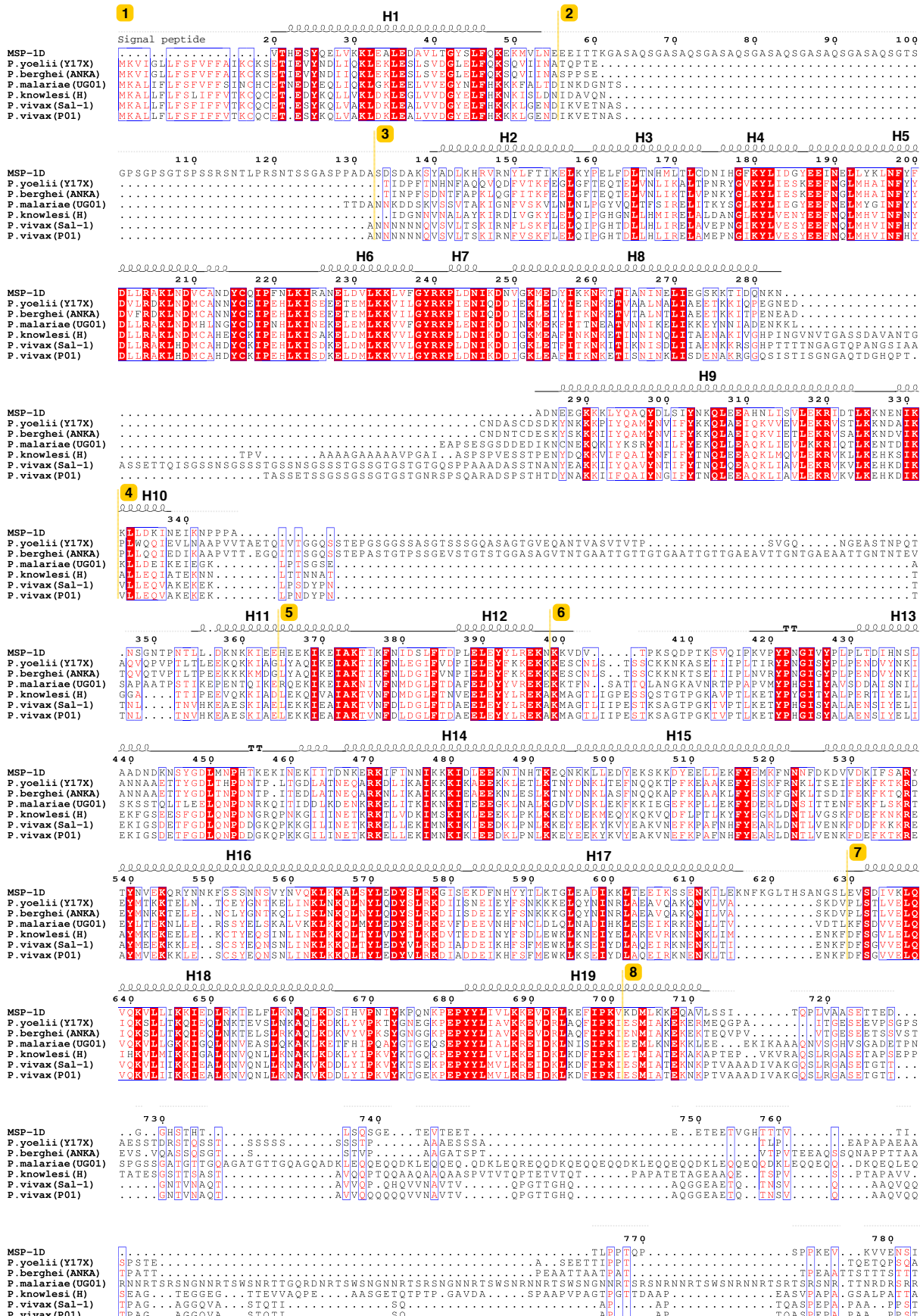


Fig. S6. Sequence alignment *P. falciparum* MSP-1. Alignment of the sequences of MSP-1 from various *P. falciparum* isolates (verified full-length sequences from Uniprot) and the MSP-1D sequence used in this study. Secondary structure as resolved for the main conformation of

the fully processed MSP-1 is shown in black; α - and β_{10} -helices are displayed as large and small squiggles, respectively; β -strands as arrows; strict β -turns and α -turns as TT and TTT, respectively; and black lines indicate resolved loops. Light dotted lines indicated unresolved stretches without predicted secondary structure. Light grey squiggles above the dotted lines indicate predicted unresolved helical secondary structure. The secondary structure of *P. falciparum* p19 (PDB accession code 1CEJ (29)) is shown underneath the alignment in grey. Sequence blocks (1-17) with various levels of homology as defined by Tanabe et al. (32) and Miller et al. (71) are indicated in yellow. Figure generated using Clustal Omega 1.2.4 (64) and ESPript 3.0 (72).



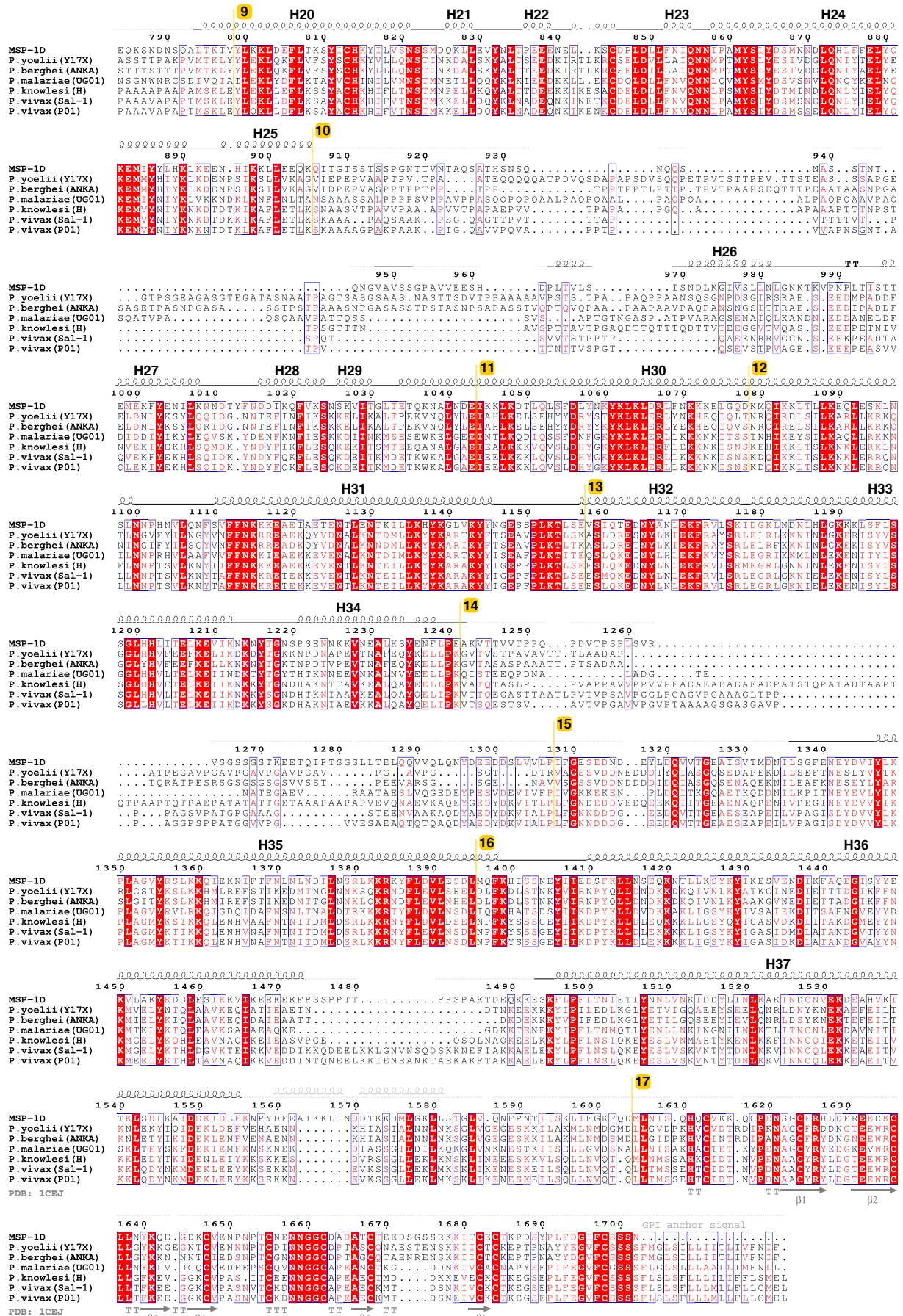


Fig. S7. Sequence alignment MSP-1 from different *Plasmodium* species. Alignment of the sequences of MSP-1 from isolates of various *Plasmodium* spp. (selected sequences as

available from PlasmoDB (63) and the MSP-1D sequence used in this study. Secondary structure as resolved for the main conformation of the fully processed MSP-1 is shown in black; α - and β_{10} -helices are displayed as large and small squiggles, respectively; β -strands as arrows; strict β -turns and α -turns as TT and TTT, respectively; and black lines indicate resolved loops. Light dotted lines indicated unresolved stretches without predicted secondary structure. Light grey squiggles above the dotted line indicate unresolved predicted helical secondary structure. Secondary structure of *P. falciparum* p19 (PDB accession code 1CEJ (29)) is shown underneath the alignment in grey. Sequence blocks (1-17) with various levels of homology as defined by Tanabe et al. (32) and Miller et al. (71) are indicated in yellow. Figure generated using Clustal Omega 1.2.4 (64) and ESPript 3.0 (72).

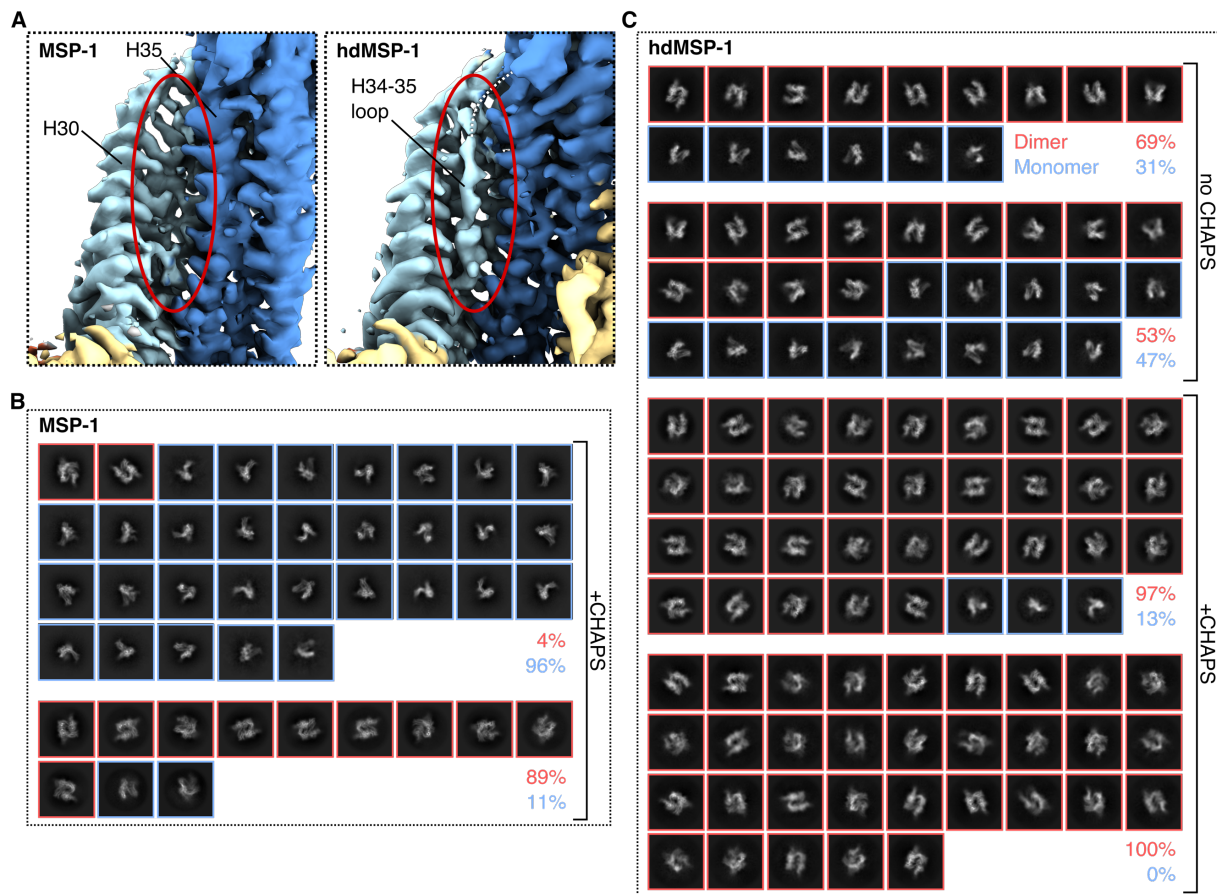


Fig. S8. Differences between MSP-1 and hdMSP-1 cryo-EM data. (A) Portion of the maps of the main conformations of MSP-1 (monomer, left) and hdMSP-1 (dimer, right) showing density in the pocket between H30 and H35 (indicated by the red oval) corresponding to the loop following H34 (part of p38) which was only resolved for the hdMSP-1 map where the connection between H34 and H35 is not cleaved by SUB-1 (the corresponding density is shown in red in Fig. 1B). The map colour indicates the corresponding MSP-1 subunit (p83, p38, and p42, in yellow, light blue, and darker blue, respectively). (B,C) 2D class averages of various data sets collected for (B) MSP-1 and (C) hdMSP-1 generated using cryoSPARC (42) (excluding classes corresponding to false-positive picks). Data sets were collected on grids prepared with or without the addition of 0.125% (w/v) CHAPS to the sample just prior to freezing. Red and blue boxes and percentages indicate classes and percentage of particles corresponding to dimeric or monomeric forms of the (hd)MSP-1 complex, respectively. The data set used to reconstruct the maps of the fully processed MSP-1 (B, top) showed mainly monomeric classes; a second control data set not used for reconstruction (B, bottom) showed more dimeric classes as seen for hdMSP-1 (C).

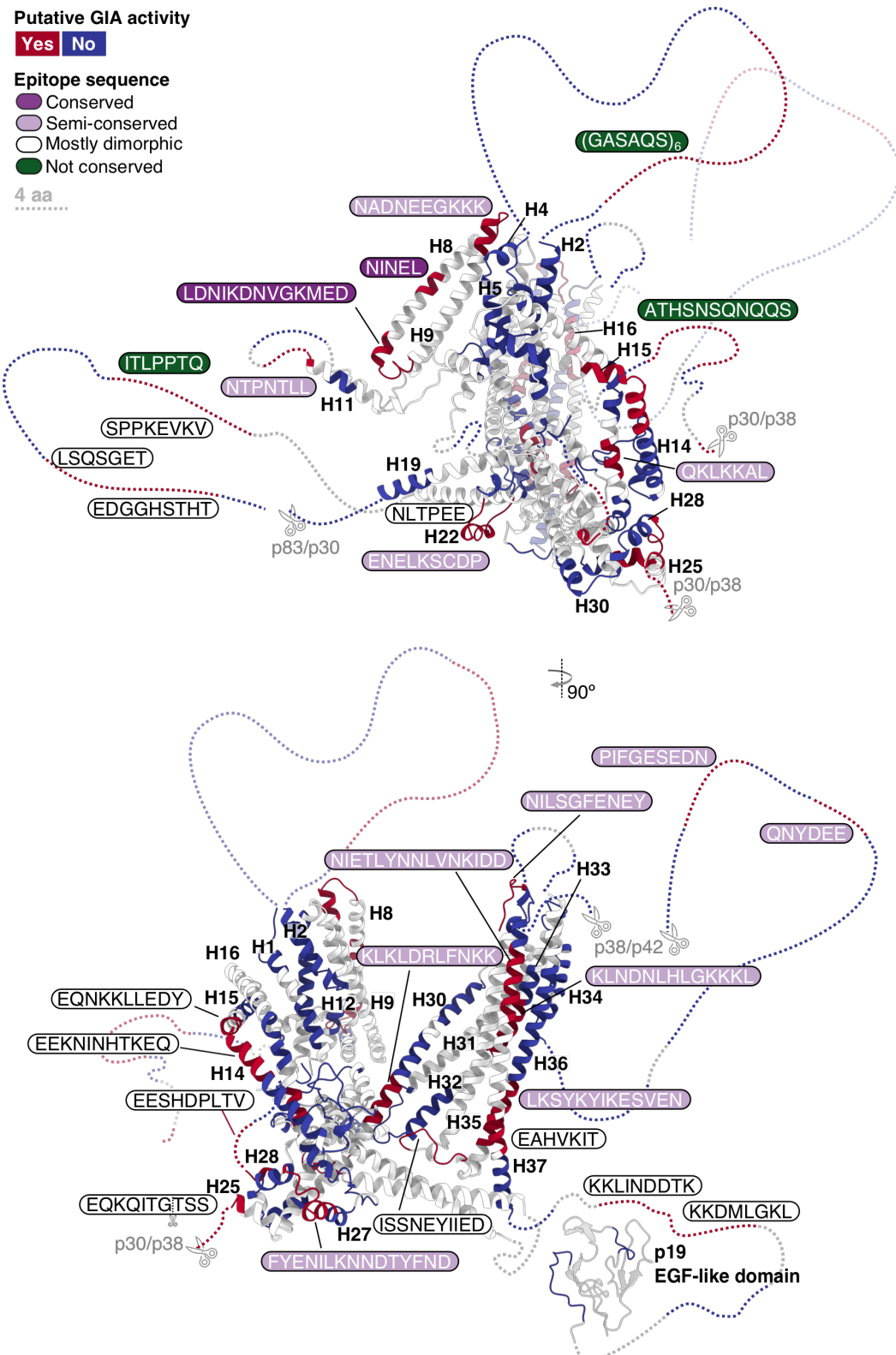


Fig. S9. Missing domains. Immunogenic B-cell epitopes recently identified in an MSP-1 vaccine trial by Blank et al. (9) are mapped onto the main conformation derived for MSP-1. In the study by Blank et al. (9), B-cell epitopes which elicited an IgG antibody response were identified in sera from vaccinees, using an MSP-1 peptide microarray chip consisting of 1,706 15-mer oligopeptides with a neighbour-to-neighbour overlap of 14 amino acids. Sera from

MSP-1-immunised rabbits and from malaria semi-immune Burkinian adults were also investigated. Based on correlation between IgG responses and parasite growth inhibition assay (GIA) activity of the various investigated sera, epitopes putatively associated with GIA activity were identified (9); blue: no role; red: possible role in inhibiting parasite growth. Epitope sequences putatively associated with GIA activity are shown and labelled according to sequence conservation: dark purple, light purple, white, and green labels correspond to conserved, semi-conserved (>50% conserved residues, rest dimorphic), mostly dimorphic (<50% conserved residues, rest dimorphic) and non-conserved epitopes. SUB-1 processing sites are marked by scissors. Same as Fig. 7, but with unresolved loops (dotted lines) drawn to scale relative to the rest of the protein in cartoon representation, and including the structure of the *P. falciparum* C-terminal EGF-like domain previously solved by nuclear magnetic resonance (PDB accession code 1CEJ (29)).

Table S1. Details of data collection and model validation.

hdMSP-1				MSP-1				
Data collection and processing								
<i>Microscope</i>	Titan Krios				Titan Krios			
<i>Magnification</i>	130,000				130,000			
<i>Voltage (kV)</i>	300				300			
<i>Detector</i>	GIF Quantum K2				GIF Quantum K2			
<i>Exposure (e⁻/Å²)</i>	60				64			
<i>Number of frames/movie</i>	40				40			
<i>Defocus range (μm)</i>	-0.5 to -3.0				-0.5 to -3.0			
<i>Pixel size (Å)</i>	1.077				1.073			
<i>Symmetry imposed</i>	C2				C1			
<i>Number of images (used/collected)</i>	12,501/15,061*				3,735/3,978			
<i>Total particles extracted</i>	2,422,429 (1,404,062)**				1,631,862 (956,925)**			
Conformation	1	2	main	Alt 1	Alt 2	Alt 3	Alt 4	Alt 5
<i>Particles refined (final)</i>	271,763	182,515	141,838	112,939	118,878	124,774	116,037	75,620
<i>Resolution unmasked (Å)</i>	4.0	4.3	4.2	4.3	4.3	4.3	4.3	7.0***
<i>Resolution masked (Å)</i>	3.3	3.6	3.1	3.3	3.2	3.2	3.2	3.6
<i>FSC threshold</i>	0.143							
<i>Sharpening B-factor (Å²)</i>	-108	-101	-77	-65	-69	-72	-70	-72
Refinement and map validation								
<i>Residues built</i>	2334	2326	1160	1160	1159	1156	1160	1159
<i>ADP (B-factor, mean, Å²)</i>	138	203	94	145	128	131	130	232
<i>Model vs half map (work)</i>	3.8	4.3	3.7	4.0	3.8	4.0	3.9	6.9****
<i>Model vs half map (free)</i>	3.8	4.2	3.8	4.1	3.9	4.0	3.9	6.9****
<i>Model vs whole map</i>	3.8	4.2	3.6	3.8	3.7	3.8	3.7	4.1
<i>FSC threshold</i>	0.5							
<i>Model vs map CC(mask)</i>	0.79	0.78	0.80	0.76	0.78	0.75	0.77	0.81
Ramachandran Plot								
<i>Favoured (%)</i>	99.30	99.30	98.68	99.21	99.12	99.21	98.95	99.03
<i>Disallowed (%)</i>	0	0	0	0	0	0	0	0
<i>Molprobity score</i>	0.87	0.90	0.79	0.82	0.77	0.84	0.82	0.78
<i>Molprobity clashscore</i>	1.38	1.54	0.97	1.13	0.87	1.23	1.13	0.92
<i>Favoured rotamers (%)</i>	98.11	98.28	98.91	98.55	98.55	98.64	98.73	98.46
<i>Poor rotamers (%)</i>	0	0	0	0	0	0	0	0
<i>EMRinger score</i>	1.56	1.33	2.18	1.66	1.75	1.36	2.21	1.31

(*Four data sets were collected on different dates for hdMSP-1 on different grids with the same settings, and subsequently merged (see fig. S2B). **Number of particles after initial 2D or 3D classification to remove false positives. ***First 0.143 threshold crossing, second at 4.0 Å. ****First 0.5 threshold crossing, second at 4.3 Å.)

Movie S1. 3D variability analysis of (hd)MSP-1 cryo-EM data showing flexibility of MSP-1.

3D variability analysis (also known as principal component analysis) was performed in cryoSPARC (51) using all particles after initial cleaning in 2D and 3D to investigate the heterogeneity in the cryo-EM MSP-1 and hdMSP-1 data sets. The movie shows a morph between the three main modes (components/eigenvectors) resolved for MSP-1 and hdMSP-1.

REFERENCES AND NOTES

1. World Health Organization, “World malaria report 2020” (ISBN 978-92-4-001579-1, World Health Organization, 2020); www.who.int/publications/i/item/9789240015791.
2. J. G. Beeson, D. R. Drew, M. J. Boyle, G. Feng, F. J. I. Fowkes, J. S. Richards, Merozoite surface proteins in red blood cell invasion, immunity and vaccines against malaria. *FEMS Microbiol. Rev.* **40**, 343–372 (2016).
3. V. L. Hale, J. M. Watermeyer, F. Hackett, G. Vizcay-Barrena, C. van Ooij, J. A. Thomas, M. C. Spink, M. Harkiolaki, E. Duke, R. A. Fleck, M. J. Blackman, H. R. Saibil, Parasitophorous vacuole poration precedes its rupture and rapid host erythrocyte cytoskeleton collapse in *Plasmodium falciparum* egress. *Proc. Natl. Acad. Sci. U.S.A.* **114**, 3439–3444 (2017).
4. R. Ladda, M. Aikawa, H. Sprinz, Penetration of erythrocytes by merozoites of mammalian and avian malarial parasites. *J. Parasitol.* **55**, 633–644 (1969).
5. P. R. Gilson, T. Nebl, D. Vukcevic, R. L. Moritz, T. Sargeant, T. P. Speed, L. Schofield, B. S. Crabb, Identification and stoichiometry of glycosylphosphatidylinositol-anchored membrane proteins of the human malaria parasite *Plasmodium falciparum*. *Mol. Cell. Proteomics* **5**, 1286–1299 (2006).
6. F. H. A. Osier, G. Fegan, S. D. Polley, L. Murungi, F. Verra, K. K. A. Tetteh, B. Lowe, T. Mwangi, P. C. Bull, A. W. Thomas, D. R. Cavanagh, J. S. McBride, D. E. Lanar, M. J. Mackinnon, D. J. Conway, K. Marsh, Breadth and magnitude of antibody responses to multiple *Plasmodium falciparum* merozoite antigens are associated with protection from clinical malaria. *Infect. Immun.* **76**, 2240–2248 (2008).
7. F. J. I. Fowkes, J. S. Richards, J. A. Simpson, J. G. Beeson, The relationship between anti-merozoite antibodies and incidence of *Plasmodium falciparum* malaria: A systematic review and meta-analysis. *PLOS Med.* **7**, e1000218 (2010).
8. J. S. Richards, T. U. Arumugam, L. Reiling, J. Healer, A. N. Hodder, F. J. I. Fowkes, N. Cross, C. Langer, S. Takeo, A. D. Ubaldi, J. K. Thompson, P. R. Gilson, R. L. Coppel, P. M. Siba, C. L. King, M. Torii, C. E. Chitnis, D. L. Narum, I. Mueller, B. S. Crabb, A. F. Cowman, T. Tsuboi, J. G.

- Beeson, Identification and prioritization of merozoite antigens as targets of protective human immunity to *Plasmodium falciparum* malaria for vaccine and biomarker development. *J. Immunol.* **191**, 795–809 (2013).
9. A. Blank, K. Fürle, A. Jäschke, G. Mikus, M. Lehmann, J. Hüsing, K. Heiss, T. Giese, D. Carter, E. Böhnlein, M. Lanzer, W. E. Haefeli, H. Bujard, Immunization with full-length *Plasmodium falciparum* merozoite surface protein 1 is safe and elicits functional cytophilic antibodies in a randomized first-in-human trial. *npj Vaccines*. **5**, 10 (2020).
10. M. J. Blackman, H.-G. Heidrich, S. Donachie, J. S. McBride, A. A. Holder, A single fragment of a malaria merozoite surface protein remains on the parasite during red cell invasion and is the target of invasion-inhibiting antibodies. *J. Exp. Med.* **172**, 379–382 (1990).
11. C. W. Kauth, U. Woehlbier, M. Kern, Z. Mekonnen, R. Lutz, N. Mücke, J. Langowski, H. Bujard, Interactions between merozoite surface proteins 1, 6, and 7 of the malaria parasite *Plasmodium falciparum*. *J. Biol. Chem.* **281**, 31517–31527 (2006).
12. G. Paul, A. Deshmukh, B. Kumar Chourasia, M. Kalamuddin, A. Panda, S. Kumar Singh, P. K. Gupta, A. Mohmmmed, V. S. Chauhan, M. Theisen, P. Malhotra, Protein-protein interaction studies reveal the *Plasmodium falciparum* merozoite surface protein-1 region involved in a complex formation that binds to human erythrocytes. *Biochem. J.* **475**, 1197–1209 (2018).
13. C. S. Lin, A. D. Ubaldi, D. Marapana, P. E. Czabotar, C. Epp, H. Bujard, N. L. Taylor, M. A. Perugini, A. N. Hodder, A. F. Cowman, The merozoite surface protein 1 complex is a platform for binding to human erythrocytes by *Plasmodium falciparum*. *J. Biol. Chem.* **289**, 25655–25669 (2014).
14. C. S. Lin, A. D. Ubaldi, C. Epp, H. Bujard, T. Tsuboi, P. E. Czabotar, A. F. Cowman, Multiple *Plasmodium falciparum* merozoite surface protein 1 complexes mediate merozoite binding to human erythrocytes. *J. Biol. Chem.* **291**, 7703–7715 (2016).
15. X. Li, H. Chen, T. H. Oo, T. M. Daly, L. W. Bergman, S.-C. Liu, A. H. Chishti, S. S. Oh, A co-ligand complex anchors *Plasmodium falciparum* merozoites to the erythrocyte invasion receptor band 3. *J. Biol. Chem.* **279**, 5765–5771 (2004).

16. R. Ranjan, M. Chugh, S. Kumar, S. Singh, S. Kanodia, M. J. Hossain, R. Korde, A. Grover, S. Dhawan, V. S. Chauhan, V. S. Reddy, A. Mohmmmed, P. Malhotra, Proteome analysis reveals a large merozoite surface protein-1 associated complex on the *Plasmodium falciparum* merozoite surface. *J. Proteome Res.* **10**, 680–691 (2011).
17. J. A. Pachebat, M. Kadekoppala, M. Grainger, A. R. Dluzewski, R. S. Gunaratne, T. J. Scott-Finnigan, S. A. Ogun, I. T. Ling, L. H. Bannister, H. M. Taylor, G. H. Mitchell, A. A. Holder, Extensive proteolytic processing of the malaria parasite merozoite surface protein 7 during biosynthesis and parasite release from erythrocytes. *Mol. Biochem. Parasitol.* **151**, 59–69 (2007).
18. C. Trucco, D. Fernandez-Reyes, S. Howell, W. H. Stafford, T. J. Scott-Finnigan, M. Grainger, S. A. Ogun, W. R. Taylor, A. A. Holder, The merozoite surface protein 6 gene codes for a 36 kDa protein associated with the *Plasmodium falciparum* merozoite surface protein-1 complex. *Mol. Biochem. Parasitol.* **112**, 91–101 (2001).
19. A. N. Hodder, P. E. Czabotar, A. D. Ubaldi, O. B. Clarke, C. S. Lin, J. Healer, B. J. Smith, A. F. Cowman, Insights into Duffy binding-like domains through the crystal structure and function of the merozoite surface protein MSPDBL2 from Plasmodium falciparum. *J. Biol. Chem.* **287**, 32922–32939 (2012).
20. R. O'Donnell, A. Saul, A. F. Cowman, B. S. Crabb, Functional conservation of the malaria vaccine antigen MSP-119 across distantly related *Plasmodium* species. *Nat. Med.* **6**, 91–95 (2000).
21. A. Combe, D. Giovannini, T. G. Carvalho, S. Spath, B. Boisson, C. Loussert, S. Thibierge, C. Lacroix, P. Gueirard, R. Ménard, Clonal conditional mutagenesis in malaria parasites. *Cell Host Microbe* **5**, 386–396 (2009).
22. M. J. Boyle, J. S. Richards, P. R. Gilson, W. Chai, J. G. Beeson, Interactions with heparin-like molecules during erythrocyte invasion by *Plasmodium falciparum* merozoites. *Blood* **115**, 4559–4568 (2010).

23. M. R. Baldwin, X. Li, T. Hanada, S.-C. Liu, A. H. Chishti, Merozoite surface protein 1 recognition of host glycophorin A mediates malaria parasite invasion of red blood cells. *Blood* **125**, 2704–2711 (2015).
24. S. Herrera, W. Rudin, M. Herrera, P. Clavijo, L. Mancilla, C. de Plata, H. Matile, U. Certa, A conserved region of the MSP-1 surface protein of *Plasmodium falciparum* contains a recognition sequence for erythrocyte spectrin. *EMBO J.* **12**, 1607–1614 (1993).
25. S. Das, N. Hertrich, A. J. Perrin, C. Withers-Martinez, C. R. Collins, M. L. Jones, J. M. Watermeyer, E. T. Fobes, S. R. Martin, H. R. Saibil, G. J. Wright, M. Treeck, C. Epp, M. J. Blackman, Processing of *Plasmodium falciparum* merozoite surface protein MSP1 activates a spectrin-binding function enabling parasite egress from RBCs. *Cell Host Microbe* **18**, 433–444 (2015).
26. U. Woehlbier, C. Epp, C. W. Kauth, R. Lutz, C. A. Long, B. Coulibaly, B. Kouyate, M. Arevalo-Herrera, S. Herrera, H. Bujard, Analysis of antibodies directed against merozoite surface protein 1 of the human malaria parasite *Plasmodium falciparum*. *Infect. Immun.* **74**, 1313–1322 (2006).
27. B. R. Ongutu, O. J. Apollo, D. M. Kinney, W. Okoth, J. Siangla, F. Dubovsky, K. Tucker, J. N. Waitumbi, C. Diggs, J. Wittes, E. Malkin, A. Leach, L. A. Soisson, J. B. Milman, L. Otieno, C. A. Holland, M. Polhemus, S. A. Remich, C. F. Ockenhouse, J. Cohen, W. R. Ballou, S. K. Martin, E. Angov, V. A. Stewart, J. A. Lyon, D. Gray Hepner Jr., M. R. Withers; MSP-1 Malaria Vaccine Working Group, Blood stage malaria vaccine eliciting high antigen-specific antibody concentrations confers no protection to young children in Western Kenya. *PLOS ONE* **4**, e4708 (2009).
28. C. W. Kauth, C. Epp, H. Bujard, R. Lutz, The merozoite surface protein 1 complex of human malaria parasite *Plasmodium falciparum*: Interactions and arrangements of subunits. *J. Biol. Chem.* **278**, 22257–22264 (2003).
29. W. D. Morgan, B. Birdsall, T. A. Frenkiel, M. G. Gradwell, P. A. Burghaus, S. E. H. Syed, C. Uthaipibull, A. A. Holder, J. Feeney, Solution structure of an EGF module pair from the *Plasmodium falciparum* merozoite surface protein 1. *J. Mol. Biol.* **289**, 113–122 (1999).

30. J. C. Pizarro, V. Chitarra, D. Verger, I. Holm, S. Pêtres, S. Darteville, F. Nato, S. Longacre, G. A. Bentley, Crystal structure of a Fab complex formed with PfMSP1-19, the C-terminal fragment of merozoite surface protein 1 from *Plasmodium falciparum*: A malaria vaccine candidate. *J. Mol. Biol.* **328**, 1091–1103 (2003).
31. Y. Ye, A. Godzik, FATCAT: A web server for flexible structure comparison and structure similarity searching. *Nucleic Acids Res.* **32**, W582–W585 (2004).
32. K. Tanabe, M. Mackay, M. Goman, J. G. Scaife, Allelic dimorphism in a surface antigen gene of the malaria parasite *Plasmodium falciparum*. *J. Mol. Biol.* **195**, 273–287 (1987).
33. P. R. Sanders, G. T. Cantin, D. C. Greenbaum, P. R. Gilson, T. Nebl, R. L. Moritz, J. R. Yates III, A. N. Hodder, B. S. Crabb, Identification of protein complexes in detergent-resistant membranes of *Plasmodium falciparum* schizonts. *Mol. Biochem. Parasitol.* **154**, 148–157 (2007).
34. R. Tolle, K. Früh, O. Doumbo, O. Koita, M. N'Diaye, A. Fischer, K. Dietz, H. Bujard, A prospective study of the association between the human humoral immune response to *Plasmodium falciparum* blood stage antigen gp190 and control of malarial infections. *Infect. Immun.* **61**, 40–47 (1993).
35. A. Jäschke, B. Coulibaly, E. J. Remarque, H. Bujard, C. Epp, Merozoite surface protein 1 from *Plasmodium falciparum* is a major target of opsonizing antibodies in individuals with acquired immunity against malaria. *Clin. Vaccine Immunol.* **24**, e00155–17 (2017).
36. D.-P. Nikodem, E.-A. Davidson, Identification of a novel antigenic domain of *Plasmodium falciparum* merozoite surface protein-1 that specifically binds to human erythrocytes and inhibits parasite invasion, in vitro. *Mol. Biochem. Parasitol.* **108**, 79–91 (2000).
37. V. K. Goel, X. Li, H. Chen, S.-C. Liu, A. H. Chishti, S. S. Oh, Band 3 is a host receptor binding merozoite surface protein 1 during the *Plasmodium falciparum* invasion of erythrocytes. *Proc. Natl. Acad. Sci. U.S.A.* **100**, 5146–5169 (2003).
38. M. A. Fierro, B. Asady, C. F. Brooks, D. W. Cobb, A. Villegas, S. N. J. Moreno, V. Muralidharan, An endoplasmic reticulum CREC family protein regulates the egress proteolytic cascade in malaria parasites. *MBio* **11**, e03078–19 (2020).

39. R. Rudolph, H. Lilie, In vitro folding of inclusion body proteins. *FASEB J.* **10**, 49–56 (1996).
40. K. Koussis, C. Withers-Martinez, S. Yeoh, M. Child, F. Hackett, E. Knuepfer, L. Juliano, U. Woehlbier, H. Bujard, M. J. Blackman, A multifunctional serine protease primes the malaria parasite for red blood cell invasion. *EMBO J.* **28**, 725–735 (2009).
41. D. Tegunov, P. Cramer, Real-time cryo-electron microscopy data preprocessing with Warp. *Nat. Methods* **16**, 1146–1152 (2019).
42. A. Punjani, J. L. Rubinstein, D. J. Fleet, M. A. Brubaker, cryoSPARC: Algorithms for rapid unsupervised cryo-EM structure determination. *Nat. Methods* **14**, 290–296 (2017).
43. J. Zivanov, T. Nakane, B. O. Forsberg, D. Kimanius, W. J. H. Hagen, E. Lindahl, S. H. W. Scheres, New tools for automated high-resolution cryo-EM structure determination in RELION-3. *eLife* **7**, e42166 (2018).
44. S. Q. Zheng, E. Palovcak, J.-P. Armache, K. A. Verba, Y. Cheng, D. A. Agard, MotionCor2: Anisotropic correction of beam-induced motion for improved cryo-electron microscopy. *Nat. Methods* **14**, 331–332 (2017).
45. A. Rohou, N. Grigorieff, CTFFIND4: Fast and accurate defocus estimation from electron micrographs. *J. Struct. Biol.* **192**, 216–221 (2015).
46. D. Asarnow, E. Palovcak, Y. Cheng, UCSF pyem v0.5 (2019).
47. E. F. Pettersen, T. D. Goddard, C. C. Huang, G. S. Couch, D. M. Greenblatt, E. C. Meng, T. E. Ferrin, UCSF Chimera — a visualization system for exploratory research and analysis. *J. Comput. Chem.* **25**, 1605–1612 (2004).
48. T. Wagner, F. Merino, M. Stabrin, T. Moriya, C. Antoni, A. Apelbaum, P. Hagel, O. Sitsel, T. Raisch, D. Prumbaum, D. Quentin, D. Roderer, S. Tacke, B. Siebolds, E. Schubert, T. R. Shaikh, P. Lill, C. Gatsogiannis, S. Raunser, SPHIRE-crYOLO is a fast and accurate fully automated particle picker for cryo-EM. *Commun. Biol.* **2**, 218 (2019).

49. Z. Yang, J. Fang, J. Chittuluru, F. J. Asturias, P. A. Penczek, Iterative stable alignment and clustering of 2D transmission electron microscope images. *Structure* **20**, 237–247 (2012).
50. M. Zhou, Y. Li, Q. Hu, X.-c. Bai, W. Huang, C. Yan, S. H. W. Scheres, Y. Shi, Atomic structure of the apoptosome: Mechanism of cytochrome *c*- and dATP-mediated activation of Apaf-1. *Genes Dev.* **29**, 2349–2361 (2015).
51. A. Punjani, D. J. Fleet, 3D variability analysis: Resolving continuous flexibility and discrete heterogeneity from single particle cryo-EM. *J. Struct. Biol.* **213**, 107702 (2021).
52. K. Cowtan, Fitting molecular fragments into electron density. *Acta Crystallogr. Sec. D Struct. Biol.* **64**, 83–89 (2008).
53. P. Emsley, B. Lohkamp, W. Scott, K. Cowtan, Features and development of *Coot*. *Acta Crystallogr. Sec. D Struct. Biol.* **66**, 486–501 (2010).
54. D. W. A. Buchan, D. T. Jones, The PSIPRED Protein Analysis Workbench: 20 years on. *Nucleic Acids Res.* **47**, W402–W407 (2019).
55. R. Sanchez-Garcia, J. Gomez-Blanco, A. Cuervo, J. M. Carazo, C. O. S. Sorzano, J. Vargas, DeepEMhancer: A deep learning solution for cryo-EM volume post-processing. *BioRxiv* 2020.06.12.148296 (2020).
56. P. D. Adams, R. W. Grosse-Kunstleve, L.-W. Hung, T. R. Iorger, A. J. McCoy, N. W. Moriarty, R. J. Read, J. C. Sacchettini, N. K. Sauter, T. C. Terwilliger, *PHENIX*: Building new software for automated crystallographic structure determination. *Acta Crystallogr. Sec. D Struct. Biol.* **58**, 1948–1954 (2002).
57. C. J. Williams, J. J. Headd, N. W. Moriarty, M. G. Prisant, L. L. Videau, L. N. Deis, V. Verma, D. A. Keedy, B. J. Hintze, V. B. Chen, S. Jain, S. M. Lewis, W. B. Arendall III, J. Snoeyink, P. D. Adams, S. C. Lovell, J. S. Richardson, D. C. Richardson, MolProbity: More and better reference data for improved all-atom structure validation. *Protein Sci.* **27**, 293–315 (2018).

58. A. J. Jakobi, M. Wilmanns, C. Sachse, Model-based local density sharpening of cryo-EM maps. *eLife* **6**, e27131 (2017).
59. T. I. Croll, *ISOLDE*: A physically realistic environment for model building into low-resolution electron-density maps research papers. *Acta Crystallogr. Sect. D Struct. Biol.* **74**, 519–530 (2018).
60. T. D. Goddard, C. C. Huang, E. C. Meng, E. F. Pettersen, G. S. Couch, J. H. Morris, T. E. Ferrin, UCSF ChimeraX: Meeting modern challenges in visualization and analysis. *Protein Sci.* **27**, 14–25 (2018).
61. A. Stivala, M. Wybrow, A. Wirth, J. C. Whisstock, P. J. Stuckey, Automatic generation of protein structure cartoons with pro-origami. *Bioinformatics* **27**, 3315–3316 (2011).
62. H. Ashkenazy, S. Abadi, E. Martz, O. Chay, I. Mayrose, T. Pupko, N. Ben-Tal, ConSurf 2016: An improved methodology to estimate and visualize evolutionary conservation in macromolecules. *Nucleic Acids Res.* **44**, W344–W350 (2016).
63. C. Aurrecoechea, J. Brestelli, B. P. Brunk, J. Dommer, S. Fischer, B. Gajria, X. Gao, A. Gingle, G. Grant, O. S. Harb, M. Heiges, F. Innamorato, J. Iodice, J. C. Kissinger, E. Kraemer, W. Li, J. A. Miller, V. Nayak, C. Pennington, D. F. Pinney, D. S. Roos, C. Ross, C. J. Stoeckert Jr., C. Treatman, H. Wang, PlasmoDB: A functional genomic database for malaria parasites. *Nucleic Acids Res.* **37**, D539–D543 (2009).
64. F. Sievers, A. Wilm, D. Dineen, T. J. Gibson, K. Karplus, W. Li, R. Lopez, H. McWilliam, M. Remmert, J. Söding, J. D. Thompson, D. G. Higgins, Fast, scalable generation of high-quality protein multiple sequence alignments using Clustal Omega. *Mol. Syst. Biol.* **7**, 539 (2011).
65. R. A. Laskowski, J. Jabłońska, L. Pravda, R. S. Vařeková, J. M. Thornton, PDBsum: Structural summaries of PDB entries. *Protein Sci.* **27**, 129–134 (2018).
66. J. Rappaport, M. Mann, Y. Ishihama, Protocol for micro-purification, enrichment, pre-fractionation and storage of peptides for proteomics using StageTips. *Nat. Protoc.* **2**, 1896–1906 (2007).

67. M. C. Chambers, B. Maclean, R. Burke, D. Amodei, D. L. Ruderman, S. Neumann, L. Gatto, B. Fischer, B. Pratt, J. Egertson, K. Hoff, D. Kessner, N. Tasman, N. Shulman, B. Frewen, T. A. Baker, M.-Y. Brusniak, C. Paulse, D. Creasy, L. Flashner, K. Kani, C. Moulding, S. L. Seymour, L. M. Nuwaysir, B. Lefebvre, F. Kuhlmann, J. Roark, P. Rainer, S. Detlev, T. Hemenway, A. Huhmer, J. Langridge, B. Connolly, T. Chadick, K. Holly, J. Eckels, E. W. Deutsch, R. L. Moritz, J. E. Katz, D. B. Agus, M. MacCoss, D. L. Tabb, P. Mallick, A cross-platform toolkit for mass spectrometry and proteomics. *Nat. Biotechnol.* **30**, 918–920 (2012).
68. M. Götze, J. Pettelkau, R. Fritzsche, C. H. Ihling, M. Schäfer, A. Sinz, Automated assignment of MS/MS cleavable cross-links in protein 3D-structure analysis. *J. Am. Soc. Mass Spectrom.* **26**, 83–97 (2015).
69. J. K. Kruschke, Bayesian estimation supersedes the t test. *J. Exp. Psychol. Gen.* **142**, 573–603 (2013).
70. E. D. Merkley, S. Rysavy, A. Kahraman, R. P. Hafen, V. Daggett, J. N. Adkins, Distance restraints from crosslinking mass spectrometry: Mining a molecular dynamics simulation database to evaluate lysine-lysine distances. *Protein Sci.* **23**, 747–759 (2014).
71. L. H. Miller, T. Roberts, M. Shahabuddin, T. F. McCutchan, Analysis of sequence diversity in the *Plasmodium falciparum* merozoite surface protein-1 (MSP-1). *Mol. Biochem. Parasitol.* **59**, 1–14 (1993).
72. X. Robert, P. Gouet, Deciphering key features in protein structures with the new ENDscript server. *Nucleic Acids Res.* **42**, W320–W324 (2014).